Lawrence Berkeley National Laboratory

Title

Facet-dependent strong metal-support interactions control the C—O bond activation

Permalink

https://escholarship.org/uc/item/7xz3r6mh

Journal

Chem Catalysis, 3(11)

ISSN

2667-1107

Authors

Shi, Song
Lee, Seungyeon
Dun, Chaochao
et al.

Publication Date

2023-11-01

DOI

10.1016/j.checat.2023.100788

Copyright Information

Peer reviewed

Facet-dependent Strong Metal Support Interactions Control the C-O Bond Activation

Song Shi[1,2§], Seungyeon Lee[1§], Chaochao Dun[3§], Weiqing Zheng[1], Jeffrey J. Urban[3], Stavros Caratzoulas[1], Dionisios G. Vlachos[1]*

Abstract

Reducible metal oxides are selective and effective C–O bond scission catalysts but are unstable under hydrogen exposure. Creating efficient redox centers while minimizing metal surfaces leads to highly selective catalysts. Single noble metal atoms activate the surface M-O bond, but the catalyst activity is limited due to low loading. Here, we report that the strong metal-support interaction (SMSI) between Ir and CeO_2 is facet sensitive, and certain facets regulate the C-O bond cleavage. At 300 °C reduction, Ir is mostly encapsulated on an octahedron by (111) facets but remains exposed by (110) facets. The former is selective whereas the latter is not. Density Functional Theory (DFT) indicates that Ir encapsulation is favored on (111) under reaction conditions, and oxygen vacancies more readily form on encapsulated Ir than on pristine ceria. This work showcases that the SMSI (encapsulation state) provides a general strategy for selective C-O bond activation.

[1] Department of Chemical and Biomolecular Engineering and Catalysis Center for Energy Innovation (CCEI), University of Delaware, Newark, DE 19716, USA.
[2] State Key Laboratory of Catalysis, Dalian Institute of Chemical Physics, Chinese Academy of Sciences, Dalian 116023, People's Republic of China.
[3] The Molecular Foundry, Lawrence Berkeley National Laboratory Berkeley, CA 94720 (USA)
[§] These authors contributed equally.

✉ email: vlachos@udel.edu

Selective C–O bond activation is essential for Fischer Tropsch synthesis, CO_2 utilization, and hydrodeoxygenation (HDO) for biomass upgrade.[1–5] Catalysts developed for C-O bond scission include metals,[6] metal oxides,[4] carbons,[7,8] and metal/acids.[9,10] Although noble metals are active, they cause inevitable side reactions. In the case of functionalized furans and aromatics from cellulose, hemicellulose, and lignin, the selectivity is low due to the metal surfaces interacting strongly with the C=C bonds of the substrates.[11] Reducible metal oxides offer much higher selectivity than metals for transforming C-O side groups, due to repelling the unsaturated rings and curtailing ring chemistry, but are unstable.

Previous mechanistic investigations revealed that the C-O bond cleavage of furan rings over metal oxides follows the reverse Mars–van Krevelen mechanism.[12] Surface oxygen vacancies, created by hydrogen during the reaction, are active redox centers selectively cleaving C–O bonds (Scheme 1). The vacancy formation rate determines the C-O bond cleaving rate. Consequently, the more reducible the surface M-O bond, the higher the rate. However, readily reducible metal oxides convert to metals. This competition between activity and stability delimits the maximum activity at high selectivity.[4] A highly efficient catalyst should have surface metal oxide reducibility but a stable bulk. For moderately reducible metal oxides, like CeO_2 and TiO_2, one can enhance the activation of the surface M-O bond by doping the oxide surface with a noble metal. However, metal nanoparticles lead to side reactions. Recently, we reported that an ultralow loading of metal dispersed into single atoms and small clusters could achieve this.[5] This strategy avoids metal-nanoparticle–catalyzed reactions while increasing the rate over the bare oxide, but the rate enhancement is suboptimal due to the low metal loading.

The classic Strong Metal Support Interaction (SMSI) concept is epitomized by a sharp reduction in the CO and H_2 adsorption after the high-temperature reduction of supported metal catalysts.[13] It usually occurs over the platinum group metals (PGMs) on reducible metal oxides, with Pt-TiO_2 being the most common pair, forming upon reduction at 500 °C. The most acceptable mechanism is encapsulation, wherein the reducible metal oxide overcoats the metal nanoparticles.[14,15] A particle size-dependent SMSI and pairs beyond PGMs and reducible oxides, such as Ni/BN,[16] Au/TiO_2,[17] and Au/MgO,[18] and adsorbate-mediated strong metal–support interactions (A-SMSI) have recently been introduced.[19] While the facets of metal oxides possess different properties, their impact on the SMSI effect is less researched, except for TiO_2.[20,21]

Here, we introduce a facet-dependent SMSI strategy for selective C-O bond activation. We expose that the SMSI between Ir and CeO_2 is facet sensitive and demonstrate that SMSI can regulate the HDO selectivity and rate. Density Functional Theory (DFT) calculations of work functions, oxygen vacancy formation energies, and binding energies

54 indicate that Ir encapsulation requires vacancies on the (111) facet and is thermodynamically preferred on the (110)
55 facet but kinetically not relevant at low reduction temperatures.
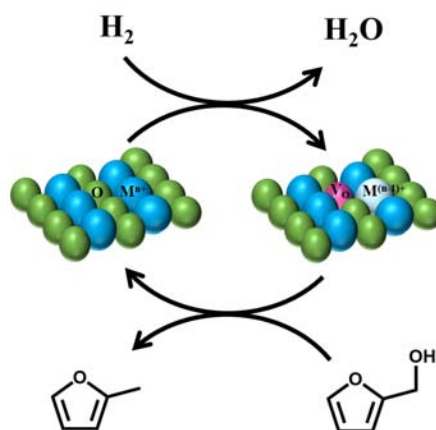
56
57 **Scheme 1.** Reverse Mars–van Krevelen mechanism for the C-O bond cleavage on a metal oxide catalyst. Oxygen vacancy (V_O) is shown in
58 pink.
59
60 **Results**
61   **Catalyst preparation and characterization**
62   CeO_2 nano-rod (CeO_2-R), nano-cube (CeO_2-C), and nano-octahedron (CeO_2-O) were prepared using
63 hydrothermal synthesis.[22] TEM and SEM images show a well-ordered morphology (Figure 1, Figure S1). XRD
64 confirms the standard CeO_2 fluorite structure (Figure S2). The TEM-inferred lattice spacings of 0.31, 0.22, and 0.19
65 nm correspond to the (111), (110), and (100) facets, respectively, consistent with the XRD data. It is generally
66 accepted that the predominantly exposed facets of CeO_2-R is the (110), of CeO_2-C is (100), and of CeO_2-O is (111)
67 (Table S1).[23–25] The surface areas, measured using N_2 adsorption/desorption, are 120, 35, and 14 m^2/g, respectively
68 (Table S1, Figure S3). Ir was impregnated with a nominal loading of 1 wt% (order of magnitude higher than typical
69 single-atom catalysts). All samples were treated at 300 °C in H_2 to reduce the metal precursor and are hereafter
70 labeled as Ir-CeO_2-X-300 (X=R, C, or O). TEM images (Figure S4-S6) show that the nanoparticles retain their
71 morphology during impregnation. The particle size of Ir on Ir-CeO_2-C-300 and Ir-CeO_2-O-300 is around 1.0 and
72 1.3 nm, respectively (Figure S5a, S6b). Ir nanoparticles were not observed on Ir-CeO_2-R-300, indicating high
73 dispersion (EDS images in Figure 1) due to the high defect density of the crystals.
74   Ir 4f peaks of Ir-CeO_2-C-300 and Ir-CeO_2-O-300 (Figure S7) show metallic Ir^0 at 60.9 eV,[26] consistent with the
75 lattice spacings of the (111) and (200) facets (Figure S6f). For the Ir-CeO_2-R-300, the peak of Ir shifts to the higher
76 binding energy of 61.3 eV, due to its high dispersion, confirmed via TEM and CO adsorption (vide infra).
77   **SMSI effect of the different CeO_2 structures**
78   The interaction of Ir and CeO_2 was studied using CO pulse adsorption, CO Drifts-IR, HR-TEM, and DFT.
79 Pretreatment can minimize the effect of CeO_2 on CO adsorption.[27] At room temperature, the CO adsorption on Ir-
80 CeO_2-R-300 reaches 40.2 mmol/g (Figure 2a, Table S2), consistent with the high dispersion of Ir, whereas on Ir-
81 CeO_2-C-300 and Ir-CeO_2-O-300, is only 4.5 and 2.0 mmol/g, respectively. These results contradict the TEM
82 showing highly dispersed Ir nanoparticles.
83   SMSI of CeO_2 typically occurs at ~700 °C.[28,29] However, SMSI can happen at as low a temperature as 300 °C
84 (same as our reduction temperature), for low loadings prepared by co-precipitation.[29] The low CO adsorption on Ir-
85 CeO_2-C-300 and Ir-CeO_2-O-300 samples suggest SMSI. To ensure full reduction of Ir, we reduced the catalyst at
86 500 °C (Figure 2b). No obvious difference on Ir-CeO_2-C and Ir-CeO_2-O was observed. Ir-CeO_2-R, on the other
87 hand, shows a classic SMSI evidenced by the dramatic CO adsorption drop at higher reduction temperatures (2
88 mmol/g at 700 °C reduction) comparable to that of Ir-CeO_2-O-300. No obvious sintering occurred during the high-
89 temperature treatment, except for a few particles (Figure S4g, h). The STEM-EDS mapping still shows highly
90 dispersed Ir, like that at 300 °C (Figure S8).
91   CO Drifts-IR (at room temperature, 1 atm of 0.3% CO/Ar) indicates a peak at 2068 cm^{-1} on Ir-CeO_2-R-300
92 from the CO adsorbing linearly on the metallic Ir (Figure 2b).[30] On Ir-CeO_2-C-300, a small peak occurs at ~2080
93 cm^{-1}.[31] The peak shift implies more interfacial sites or potential electronic interaction between the particles and
94 substrate. On the Ir-CeO_2-O-300, only gas-phase peaks are detected. Considering the decreased CO adsorption of
95 Ir-CeO_2-R with increasing reduction temperature, *in-situ* Drifts-IR of CO at various reduction temperatures was
96 conducted (Figure 2c). The CO adsorption peaks gradually decrease and ultimately disappear at 700 °C and the

peak at 2068 cm^{-1} (300 $^{\circ}$C reduction) shifts to 2080 cm^{-1} (500 $^{\circ}$C reduction), probably due to the electronic interaction of Ir and CeO$_2$ (a characteristic of SMSI).
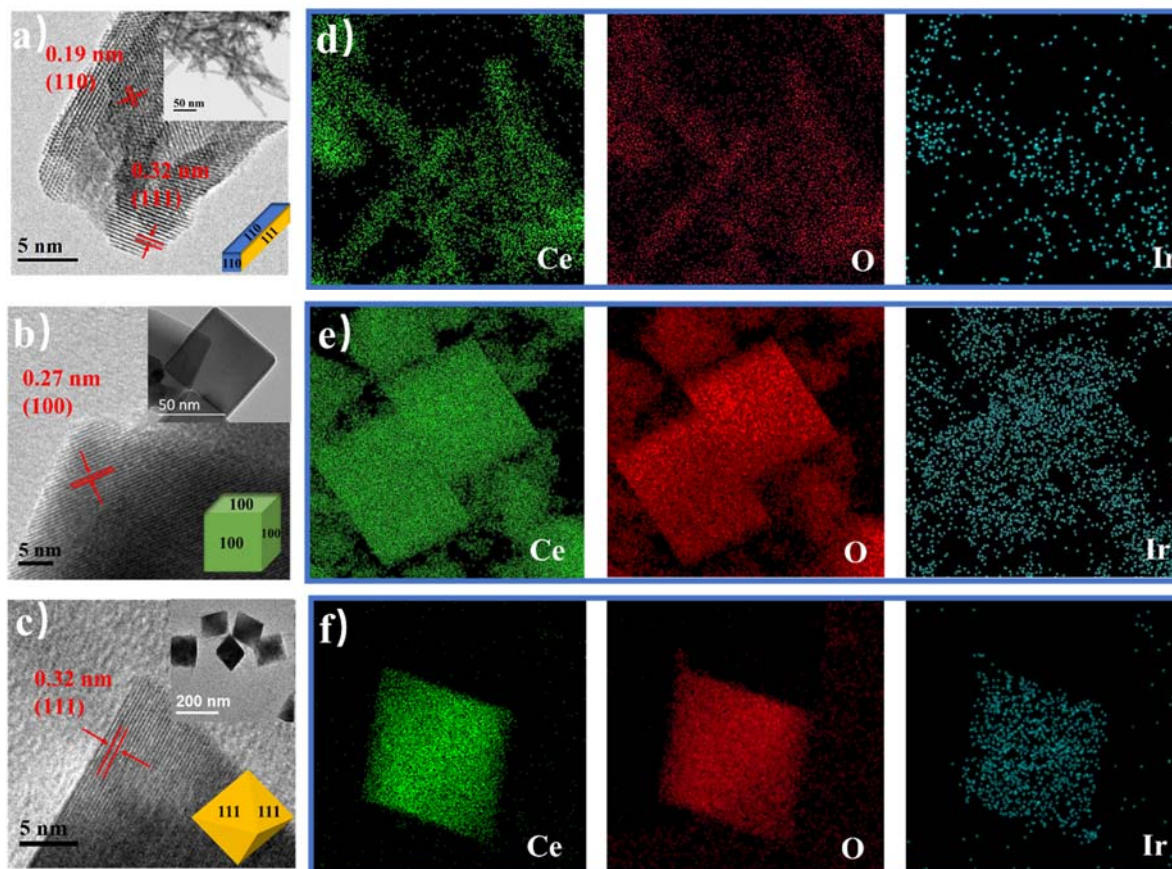
Figure 1. Microscopy characterization and elemental mapping. TEM images of a) CeO$_2$-R, b) CeO$_2$-C, c) CeO$_2$-O, HAADF-STEM images, and corresponding EDX elemental mappings: d) Ir-CeO$_2$-R-300, e) Ir-CeO$_2$-C-300, f) Ir-CeO$_2$-O-300.

HR-TEM images show thin oxide layers over the Ir nanoparticles. On Ir-CeO$_2$-O-300, nearly all Ir particles were encapsulated by CeO$_2$ (Figure 2d, S6c-f). On Ir-CeO$_2$-C-300, they were only partially encapsulated (Figure S5c), enabling a slight CO adsorption (Figure 2a). Ir on Ir-CeO$_2$-R-700 remains highly dispersed (Figure S8); a tiny amount aggregates and is encapsulated by amorphous CeO$_2$ (Figure S4f). In addition, amorphous layers of Ir-CeO$_2$-O-300 without Ir after hydrogen reduction form, implying surface reconstruction (Figure S6a). This surface reconstruction is likely responsible for the SMSI effect.

The above spectroscopic and microscopy results demonstrate that the SMSI effect sensitively depends on the CeO$_2$ facet, a phenomenon not previously documented for CeO$_2$. Prior studies have suggested that smaller metal particles require higher reduction temperatures for encapsulation. To partially rule out size effects on various facets, control experiments were performed by loading the same size of Ir particles (~1 nm, Figure S9) on Ir-CeO$_2$-R-np, Ir-CeO$_2$-C-np, and Ir-CeO$_2$-O-np. CO adsorption shows a similar trend as direct impregnation (Table S2, entries 14-20). HR-TEM images highlight that the Ir particles on the Ir-CeO$_2$-O-np are also encapsulated by an amorphous shell (Figure S10d), indicating that the SMSI effect is independent of the initial Ir state. On Ir-CeO$_2$-R-np, despite some bare Ir particles (Figure S10b), most Ir nanoparticles are highly re-dispersed as in impregnation (Figure S10a). Increasing the reduction temperature to 700 $^{\circ}$C encapsulates the Ir nanoparticles (Figure S10c), like the impregnation. We conclude this facet-dependent SMSI effect is weakly size-dependent over our studied particle size range.

To further understand the encapsulation, we performed DFT calculations. For encapsulation to be thermodynamically favorable between a metal and an oxide support, (i) the surface energy of the oxide has to be lower than that of the metal; and (ii) the work function of the oxide has to be smaller than that of the metal as, then, electron transfer from the oxide to the metal surface results in upward band bending at the oxide interface while the positive electric field out of the oxide promotes migration of the oxide's cations.[32,33]

The surface energies are: $CeO_2(111)$, 0.71 J/m^2 < $CeO_2(110)$, 1.00 J/m^2 < $CeO_2(100)$, 1.45 J/m < Ir(111), 2.50 J/m^2.[34] Based on these, Ir encapsulation by $CeO_2(111)$ is more likely than by $CeO_2(110)$ or $CeO_2(100)$. Next, the work function (Φ) at dilute oxygen vacancy (V$_O$) concentration is compared with Ir(111) (Figure 2e). On pristine CeO_2, only (110) favors Ir encapsulation ($\Phi_{CeO2(110)} < \Phi_{Ir(111)}$), while (100) is the least likely ($\Phi_{CeO2(100)} > \Phi_{Ir(111)}$). Upon forming a single V$_O$, Φ of $CeO_2(111)$ decreases (6.14 eV for pristine, 5.06 eV with V$_O$, Table S3) below that of Ir(111), making encapsulation favorable. The work function of $CeO_2(111)$ and $CeO_2(110)$ decreases with the V$_O$ concentration, in agreement with previous reports,[35] while Φ of $CeO_2(100)$ is rather independent of the V$_O$ concentration and greater than Φ of Ir(111), suggesting that encapsulation by $CeO_2(100)$ is unlikely. Our data indicate that $CeO_2(110)$ is most likely to promote Ir encapsulation, while a small amount of V$_O$ in $CeO_2(111)$ is necessary for encapsulation.

We hypothesize that encapsulation of Ir by $CeO_2(110)$ does not occur readily at low reduction temperatures, despite the favorable difference in Φ. The reason is that the top layer of $CeO_2(110)$ exposes the less coordinated Ce$_{6c}$ atoms which function as intrinsic defects,[36] whereas $CeO_2(111)$ exposes evenly spaced Ce$_{7c}$ atoms (Supplemental Note S1, Figure S11-S13). At high reduction temperatures, Ir encapsulation is also observed for Ir-CeO_2-R (e.g., Ir-CeO_2-R-700), as anticipated by the difference in Φ (Figure 2e) and supported by CO adsorption (Figure 2a) and HR-TEM images (Figure S4f). The significantly higher surface area of $CeO_2(110)$ than that of $CeO_2(111)$ (120 vs 14 m^2/g, Table S1) inhibits Ir aggregation. Lastly, we re-emphasize that while the (110) is the most exposed facet of CeO_2-R, the presence of (111) or (100) facets must be kept in mind. There is an ongoing debate as to which two facets compose CeO_2-R ((110)+(111) vs. (110)+(100)).[23–25] Nevertheless, the (111) or (100) will reduce the probability of Ir encapsulation on CeO_2-R.
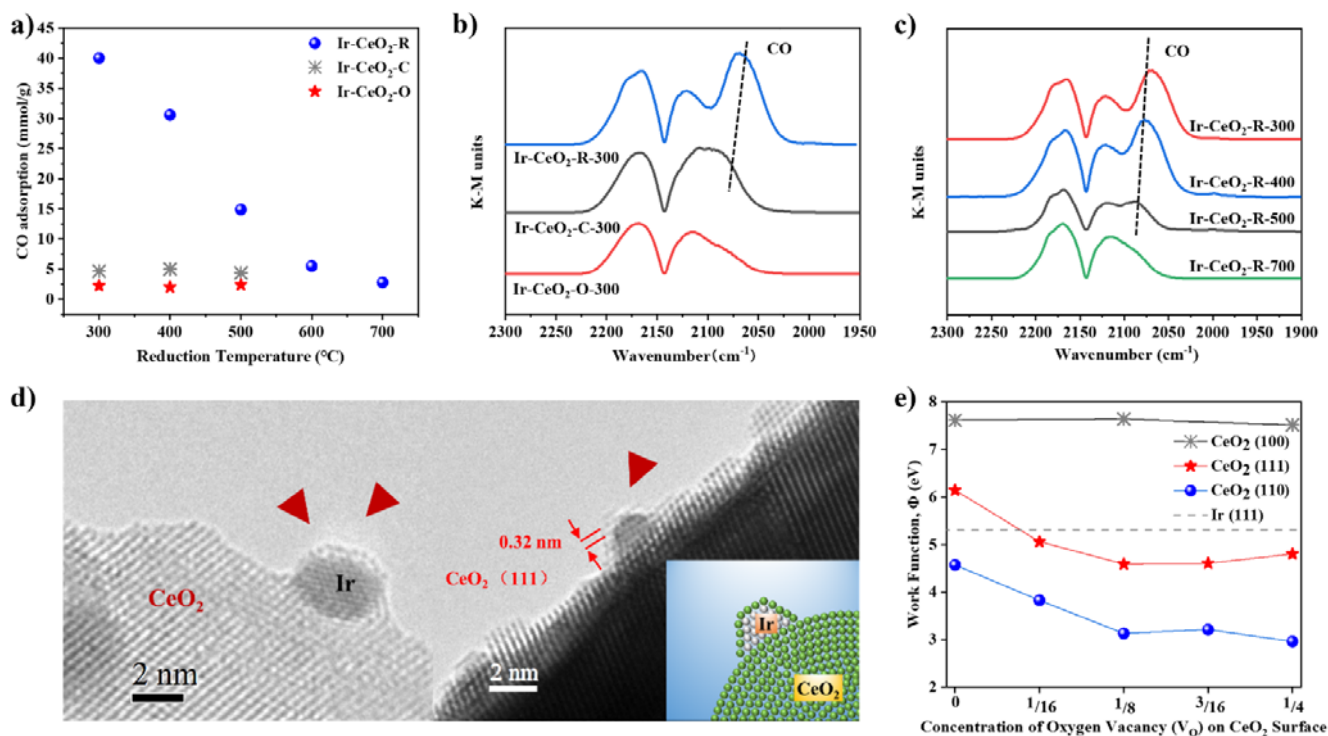
Figure 2. Spectroscopic characterization, high-resolution imaging, and work function (Φ). a) CO adsorption amount on different catalysts, b) *In-situ* Drifts-IR of CO on different CeO_2 supported catalysts, c) *in-situ* Drifts-IR of CO of Ir-CeO_2-R under different reduction temperatures, d) HR-TEM images of Ir-CeO_2-O-300. e) Computed work functions (Φ) for CeO_2 facets with varying concentrations of oxygen vacancies (V$_O$). Gray dashed line is the work function of Ir(111). Work function values are reported in Table S3.

Application to the HDO of furfuryl alcohol

HDO of furfuryl alcohol was employed as a model reaction to study the facet effect on the C-O bond cleavage. The chemistry entails C-O bond cleavage to 2-methyl furan (2-MF) and ring chemistry (hydrogenation and opening) (Figure S14). Consistent with previous work on reducible oxides, the three CeO_2 catalysts (without Ir) show high selectivity to HDO, with no ring hydrogenation,[4] and different rates for C-O bond activation: CeO_2-R is the most active and CeO_2-O the least (Figure S15). The rates, after normalizing with the surface area (Figure 3a), are within a factor of two, following the order CeO_2-O < CeO_2-C < CeO_2-R.
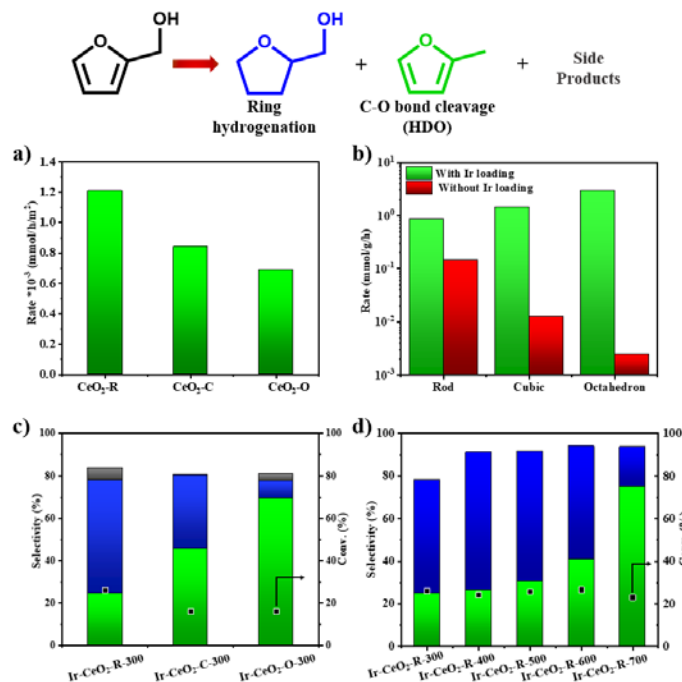
Figure 3. Catalyst evaluation in HDO over different catalysts. Top: schematic of reactions. a) HDO rate normalization with surface areas of CeO_2 on different facets. b) HDO rate of CeO_2 before and after Ir loading. c) Performance of different CeO_2-supported Ir catalysts. d) Performance of Ir-CeO_2-R catalyst reduced at different temperatures. Reaction conditions, 1 mmol furfuryl alcohol in 10 ml isopropanol, reaction temperature at 180 °C, 300 psi H_2 measured at room temperature. Green and red bars: 2-methyl furan, Blue bars: furfuryl alcohol, Gray bars: others.

The catalytic performance changes dramatically upon loading Ir on CeO_2 (Figure 3b). At a similar conversion, the selectivity of the products on Ir-CeO_2-O-300 is dominated by 2-MF (Figure 3c), while on Ir-CeO_2-R-300, the ring hydrogenation product, tetrahydrofurfuryl alcohol, dominates. The selectivity on Ir-CeO_2-C-300 is comparable to that of the other two catalysts. The rate increases upon loading Ir (Table S4, Figure 3b, S14). On Ir-CeO_2-O-300, it rises by almost three orders over the pristine oxide (from 0.0024 to 2.92 mmol/g/h), as Ir facilitates the Ce-O bond activation, forming HDO redox centers. The rate follows Ir-CeO_2-R < Ir-CeO_2-C < Ir-CeO_2-O, which is opposite of the pristine CeO_2. These performance differences stem from the SMSI effect stated above.

The selectivity differences can be attributed to the facet-dependent encapsulation. The metal surface is the primary site for ring hydrogenation.[5,37,38] Ir-CeO_2-R-300 possesses the highest amount of metallic Ir sites, evidenced by CO adsorption and Drifts-IR, resulting in the most ring hydrogenation. Conversely, Ir-CeO_2-O-300 shows low ring hydrogenation due to the full encapsulation of Ir nanoparticles and minimally exposed metal. This is consistent with the slower hydrogenation for Ir-CeO_2-R when the metallic sites are reduced via higher temperature reduction (Figure S17). Since the metal oxide or the metal/metal oxide interface could also be active, even when encapsulated by the CeO_2, the Ir-CeO_2-O-300 still promotes C-O bond cleavage. These phenomena were also confirmed on Ir-CeO_2-R at various reducing temperatures (Figure 3d). By increasing the reduction temperature, ring hydrogenation decreases due to the decreased number of metallic sites (Figure S17). At 700 °C reduction temperature, the C-O bond cleavage dominates, consistent with the encapsulation (Figure 2a) occurring at 700 °C. The Ir-CeO_2-C and Ir-CeO_2-O state are insensitive to the reduction temperature, maintaining a constant selectivity (Figure S18).

Unlike single atoms catalysis, the SMSI effect is fairly insensitive to the loading.[39] For CeO_2-O, even with a loading of 4 wt%, the C-O bond cleavage dominates (Figure S19). These results clearly show that the SMSI effect is an excellent knob to regulate selectivity.

Given the HDO rate is strongly affected by the oxygen vacancies, Raman, XPS, and H_2 TPR were used to explore the different morphologies systematically. In CeO_2, the Raman peak at 460 nm^{-1} corresponds to the octahedral symmetry of the lattice, while peaks at 598 nm^{-1} show the defect-induced mode (Figure S20).[23] The peak ratio of I_{598}/I_{462}, indicative of the oxygen vacancy density on the surface, followed the order CeO_2-O < CeO_2-C < CeO_2-R, rationalizing the reaction rate ranking. The oxygen vacancy density is also supported from XPS analysis of Ce and O (Figure S21).[40] For Ce 3d, peaks at 881.2, 884.9, 899.3, and 903.1 eV are attributed to Ce^{3+} species and the rest to Ce^{4+}. The Ce^{3+} to Ce^{4+} species in CeO_2-R and CeO_2-O are 45.1 and 39.3%, respectively (Table S5). For O 1s, the peaks at 529.3 eV are due to the lattice oxygen and at 531.8 eV to the chemisorbed oxygen or oxygen vacancies.[41,42] The latter is more active compared with the lattice oxygen according to the XPS peak shift. Thus, its

198 ratio can still be used to estimate the efficient redox center. For CeO_2-R and CeO_2-O, the ratio of chemisorbed
199 oxygen is 52.2 and 49.7%, respectively (Table S5). XPS results of Ce 3d and O 1S support that the oxygen vacancy
200 density follows the order CeO_2-O < CeO_2-C < CeO_2-R, consistent with the Raman results above. H_2 TPR further
201 confirms the oxygen vacancy difference. Figure S22 shows two peaks in the three CeO_2 samples; the lower
202 temperature one is assigned to surface Ce and the one at ~600 °C to the bulk oxide reduction.[43] The shift in the
203 lower temperature peak, from 520 to 480 to 400 °C for CeO_2-O, CeO_2-C, and CeO_2-R, underscores the efficacy of
204 reducing the various oxide facets, and its nice correlation to the facet-sensitive HDO rate and the reverse Mars–van
205 Krevelen mechanism.

206   Metal doping is effective for activating the lattice oxygen and forming redox centers.[44–46] The I_{598}/I_{460} ratio of
207 the Raman data (Figure 4a) follows the trend Ir-CeO_2-R-300 < Ir-CeO_2-C-300 <Ir-CeO_2-O-300. The XPS data
208 (Figure 4b-c, S23-25, Table S6-8) shows that the Ce^{3+} species ratio increases from 46.3 to 57.0% and the
209 chemisorbed oxygen ratio from 83.1 to 159.0%, consistent with the Raman data. The XPS data also follows a
210 similar trend for the nanoparticle deposition method (Figure S26, Table S9), suggesting this oxygen vacancy
211 difference is highly related to its intrinsic nature. Similarly, this trend was further confirmed by H_2 TPR (Figure 4d,
212 S27). The peaks below 200 °C are due to the reduction of Ir, and the ones at 200-350 °C to the newly formed redox
213 centers. Compared with pristine CeO_2, all samples are reduced at lower temperatures due to being activated by Ir.
214 In contrast to the Ir-CeO_2-R catalyst (Figure S28a-b) which exhibits aggregation, the Ir-CeO_2-O is stable and can
215 be recycled at least three times (Figure S29).
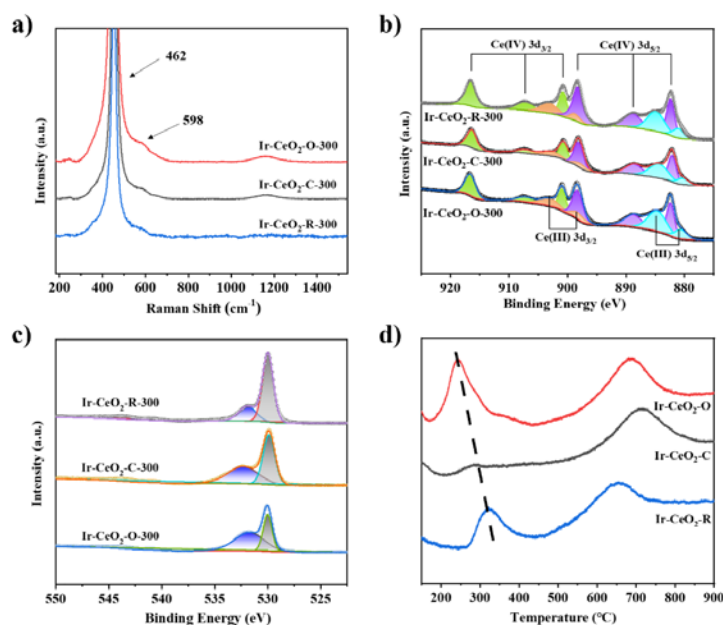
**Figure 4. Raman, XPS, and catalyst reduction data.** a) Raman spectra of Ir-CeO_2-R-300, Ir-CeO_2-C-300, and Ir-CeO_2-O-300 b), c) XPS
spectra and corresponding fitting curves of Ce 3d and O 1s in Ir-CeO_2-R-300, Ir-CeO_2-C-300, and Ir-CeO_2-O-300, Ce^{3+} species (881.2, 884.9,
899.3 and 903.1 eV), Ce^{4+} species (882.2, 888.2, 898.1, 900.7, 907.3, and 916.7 eV), chemisorbed oxygen (531.8 eV), lattice oxygen (529.3
eV). d) H_2 TPR of Ir-CeO_2-R, Ir-CeO_2-C, and Ir-CeO_2-O.

225   Next, we calculate the oxygen vacancy formation energy (E_{V_o}) and the adsorption energy of CO and furfuryl
226 alcohol (FA) on Ir-CeO_2-O and Ir-CeO_2-R and compare them with the "pristine" surfaces (see Supplemental Note
227 S2, Table S10-14, Figure S30-32). The Ir-CeO_2-O-300 model was informed by the TEM images and XPS
228 measurements, which showed Ir^0 (111) encapsulation under a thin layer of CeO_2. Ir(111) partially covered (4/9 or
229 2/3 of the surface) to fully covered (mono or bilayer) by CeO_2 (111) (Figure 5a) represents Ir-CeO_2-O (hereafter
230 θ•CeO_2, where θ = 4/9, 2/3, 1 or 2). Overall, only 1•CeO_2 (hereafter Ir-O) has E_{V_o} lower than CeO_2(111) and
231 effectively reflects the higher concentration of Ce^{+3} species in Ir-CeO_2-O-300 (36.2%, Table S8) compared to CeO_2-
232 O (28.2%, Table S5). For the Ir-CeO_2-R-300 model, $Ir^{+δ}$ is slightly cationic and uniformly distributed on CeO_2-R.
233 Different configurations of Ir_n (n = 1– 5) were introduced in CeO_2(110) to investigate atomically dispersed Ir and
234 small nanoclusters. Only Ir_1 (hereafter referred to as Ir-R) has E_{V_o} similar to that of pristine CeO_2(110) (1.34 vs
235 1.35 eV), while the V_O's for Ir_{2-5} requires more energy than pristine CeO_2(110), as shown in Figure 5b (1.63–2.62

236 eV vs 1.35 eV, Table S13). The comparable E_{V_o} between the CeO$_2$(110) and Ir-R captures the minimal change in
237 V_O densities observed for CeO$_2$-R-300 (31.1 % of Ce^{+3}, Table S5) and Ir-CeO$_2$-R-300 (31.6% of Ce^{+3}, Table S6).
238
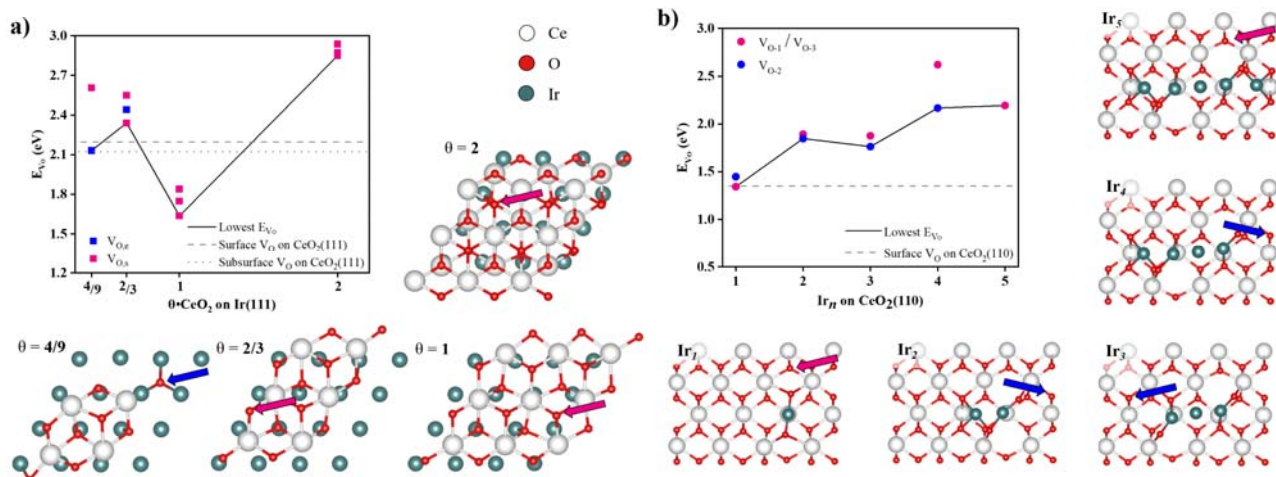
239
240 **Figure 5. Oxygen vacancy formation energies (E_{V_o}) of θ•CeO$_2$ (θ = 4/9, 2/3, 1, 2) layers relaxed on Ir(111) (a) and Ir$_n$ (n = 1-5) on**
241 **CeO$_2$(110) (b) to model Ir-CeO$_2$-O and Ir-CeO$_2$-R, respectively.** The surface geometries are displayed next to the plots (only the top
242 surface is shown). Two different types of oxygens are removed for the two models (shown in pink/blue squares/circles). A solid black line
243 highlights the lowest E_{V_o} per model of varying coverage or metal loading (blue/pink arrows indicate the corresponding oxygen removed).
244 Gray dashed lines indicate E_{V_o} of pristine CeO$_2$. All E_{V_o} values are reported in Table S12 and Table S13 for (a) and (b), respectively.
245

246 We investigated the binding of CO and furfuryl alcohol (FA) on *Ir-O* and *Ir-R* with an oxygen vacancy as XPS
247 data showed Ce^{+3} cations on Ir-CeO$_2$-R-300 and Ir-CeO$_2$-O-300 (Figure 4b-c). CO pulse adsorption implied
248 exposed Ir atoms on Ir-CeO$_2$-R-300 (Figure 2a). This is reflected in the stronger CO adsorption on *Ir-R* ($E_{ad,CO}$ = -
249 1.62 eV) than on *Ir-O* ($E_{ad,CO}$ = -0.40 eV) due to the direct binding of CO to the exposed Ir metal in *Ir-R*. In addition,
250 we computed weaker CO adsorption on *Ir-R* than on Ir(111) (-2.02 eV) and stronger adsorption on *Ir-O* than on
251 CeO$_2$ (~0 eV) (Table 1, Figure S29), reflecting changes in the electronic properties.
252 Next, the binding via the -OH group and the furan ring (C=C) was assessed on different surfaces. Oxide surfaces
253 favor the adsorption of the -OH group and are selective for HDO, while metal surfaces bind the furan ring.[47] This
254 is verified by the preferred adsorption geometries on CeO$_2$ and Ir (Table 1). Upon introducing Ir in CeO$_2$, we
255 observe a strong preference for binding via the OH group on *Ir-O* ($E_{ad,FA}$ = -2.47 eV via the OH group) and via the
256 furan ring on *Ir-R* ($E_{ad,FA}$ = -0.95 eV via the ring vs -0.79 eV via the OH group). The preferred binding geometries
257 on *Ir-R* and *Ir-O* agree with the observed enhancement in hydrogenation and HDO activity on Ir-CeO$_2$-R-300 and
258 Ir-CeO$_2$-O-300 (Figure 3c).
259
260 **Table 1.** The adsorption energy of CO and furfuryl alcohol (FA) on Ir and CeO$_2$ surfaces with an V_O. The CO and FA adsorption geometries
261 are presented in Figure S33. ($E_{ad,CO\ or\ FA}$ = $E_{surf.w.CO\ or\ FA}$ − $E_{surface}$ − $E_{CO\ or\ FA(gas)}$)

	$E_{ad,CO}$ (eV)	$E_{ad,FA}$ (eV) via	
		Furan ring (C=C)	Alcohol (-OH)
Ir (111)	-2.02	-2.57	N/A
CeO$_2$ (111)	-0.05	-1.03	-1.65
CeO$_2$ (110)	0.06	-1.05	-1.27
Ir-O	-0.40	-0.94	-2.47
Ir-R	-1.62	-0.95	-0.79

262
263 In summary, these experiments and DFT results highly suggest that upon adding Ir, the C-O bond cleavage rate is
264 determined by the oxygen vacancies by the reverse Mars–van Krevelen mechanism.
265
266 **Discussion**
267 The SMSI effect was discovered long ago, yet, the mechanism is still investigated. Recently, new SMSI effects
268 have been discovered.[48–51] Oxide facets are important and TiO$_2$ was the first reported facet-sensitive material in
269 SMSI.[21] Here, we firstly reported that the SMSI effect of Ir and CeO$_2$ is facet controlled. The (111) facet more
270 readily forms an encapsulated state at a low reduction temperature of 300 °C, far lower than the traditional 700 °C

271 of CeO_2. DFT calculations also revealed that Ir encapsulation is likely to occur into $CeO_2(110)$ and $CeO_2(111)$ with
272 oxygen vacancies, but unlikely to occur into $CeO_2(100)$ due to the difference in the work functions (Figure 2e).

273 　　　Owing to the encapsulation of the metal nanoparticles, SMSI usually decreases the rate of catalytic reactions
274 but exceptions have been reported.[21,29,52,53] Until now, little attention has been paid to controlling the C-O bond
275 scission via the SMSI effect.[54] A facet-controlled SMSI effect enables the metal in different encapsulation states.
276 Encapsulation does not expose the metallic surface, staving off the side reactions such as the ring chemistry, but
277 provides more redox centers for HDO. Unlike the traditional loading method,[55] the whole thin layers over the noble
278 metal particles could be activated, changing the sites from the 2D perimeter to 3D. Here, Ir is almost fully
279 encapsulated on the octahedron CeO_2 and possesses the highest selectivity toward the C-O cleavage and the highest
280 C-O bond rate due to the highest oxygen vacancy density (Scheme 2).

281 　　　DFT revealed that a single oxygen vacancy forms easier in *Ir-R* than *Ir-O* (E_{V_o} = 1.34 eV vs. 1.64 eV), while
282 HDO activity is higher on $Ir-CeO_2-O-300$ than on $Ir-CeO_2-R-300$. Moderate E_{V_o} values are preferable for high
283 activity as catalysts with low E_{V_o} values have a higher energy cost associated with surface regeneration.[4] We found
284 that oxygen vacancies form more readily in *Ir-O* (E_{V_o} = 1.64 eV) than in pristine $CeO_2(111)$ (E_{V_o} = 2.20 eV) and
285 prefer the -OH group of FA over the furan ring. Moreover, *Ir-O* has a larger active site, encapsulating the entire 3D
286 surface of Ir (Scheme 2) compared to *Ir-R* which is atomically dispersed, and the active site is restricted to the Ir-
287 CeO_2 interface. Moderate E_{V_o} and large active area of *Ir-O* compensate for the higher activity compared to *Ir-R* of
288 low E_{V_o} and smaller active area. The proposed strategy could be extended to other metal/metal oxide pairs.

2D perimeter　　　3D thin layer
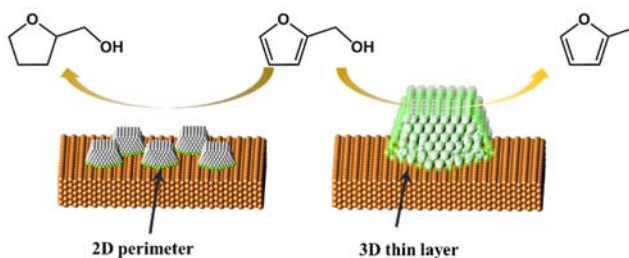
289
290 **Scheme 2.** Proposed reaction mechanism and depiction of active sites.
291

292 **Methods**
293 **Preparation of catalysts**
294 *The CeO_2-rod (CeO_2-R) synthesis*
295 4 mmol $Ce(NO_3)_2 \cdot 6H_2O$ was dissolved in 80 ml 6 M NaOH aqueous solution, stirred for 20 min, and then placed in a hydrothermal synthesis
296 reactor at 100 °C for 24 h. The obtained solid was washed with water until neutral and then calcined at 350 °C for 6 hours.
297 *The CeO_2-cubic (CeO_2-C) synthesis*
298 4 mmol $Ce(NO_3)_2 \cdot 6H_2O$ was dissolved in 80 ml 6 M NaOH aqueous solution, stirred for 20 min, and then placed in a hydrothermal synthesis
299 reactor at 180 °C for 24 h. The obtained solid was washed with water for 6 times and calcined at 350 °C for 6 hours.
300 *The CeO_2-octahedron (CeO_2-O) synthesis*
301 2 mmol $Ce(NO_3)_2 \cdot 6H_2O$ dissolved in 80 ml 0.02 mM Na_3PO_4 aqueous solution, stirred for 20 min, and then placed in a hydrothermal
302 synthesis reactor at 　170 °C for 12 h. The obtained solid was washed with water 6 times, and then calcined at 350 °C for 6 hours.
303 *$Ir-CeO_2$ synthesis*
304 The CeO_2-supported Ir catalysts were prepared using incipient wetness impregnation. Typically, CeO_2 was dispersed in the 1.0 wt % H_2IrCl_6
305 solution. The Ir loading was 1.0 wt%. Then the catalysts were reduced under pure H_2 for 6 hours. For the Ir nanoparticles, 4 mL of a solution
306 of NaOH at 0.5 M in ethylene glycol with an equal volume of a solution of $H_2IrCl_6 \cdot 6H_2O$ at 20 mM in EG was placed in a 20 ml vial. The
307 NaOH/Ir molar ratio is 25. The vials were replaced with N_2 and heated to 170℃ for 3 hours. The obtained Ir nanoparticles were washed with
308 HCl and re-dispersed in ethanol. To load them on CeO_2, a certain amount of CeO_2 was added into the solution, dried on the hotplate, and
309 then reduced under pure H_2 at a certain temperature for 6 hours.
310 **Characterization.** X-ray photoelectron spectroscopy (XPS) was performed on a Thermofisher ESCALAB 250Xi spectrometer using AlKα
311 radiation. The binding energies were calibrated using the C 1s level (284.8 eV). ^{13}C cross-polarization magic-angle spinning nuclear magnetic
312 resonance (^{13}C CP/MAS NMR) spectra were collected on Bruker AVANCE III HD 600 MHz. *In situ* Drifts spectroscopy measurements
313 were conducted on a Nicolet 6700 instrument equipped with a Harrick drifts cell. ATR measurements of the catalysts were conducted on a
314 Nicolet 6700 instrument equipped with golden state ATR accessories. The TEM images are obtained using the JEM2010F and JEM2100F.
315 The SEM images are recorded by Zeiss Auriga 60 High Resolution Focused Ion Beam & Scanning Electron Microscope. XRD patterns are
316 collected on Bruker D8 with Cu K α radiation. N_2 adsorption isotherm is collected on Micromertics ASAP 2020 BET Analyzer. The CO
317 pulse adsorption and H_2 TPR experiment are performed using a Micromertics ASAP 2020 BET Analyzer, before the CO pulse adsorption,
318 catalysts were reduced at 300 °C.
319 **Reaction procedures and products analysis.** Catalytic reactions were performed in a 125 mL autoclave reactor. Typically, 50 mg catalyst
320 and 10 mL IPA containing 1% furfural alcohol were added into the reactor. Then, the reactor was charged with 300 psi H_2 and heated to the
321 desired temperature under magnetic stirring. When the reaction was complete, the reactor was quenched with the ice bath, and then a small
322 amount of trimethyl benzene was added as an internal standard. The products were identified using an Agilent 7890N GC/5973 MS detector
323 and quantitated by Agilent 7890N GC equipped a CP-Volamine (30.0 m × 0.320mm) column and flame ionization detector (FID).

Density-Functional Theory (DFT) Calculations

Spin-polarized periodic-DFT calculations were performed at the Perdew-Burke-Ernzerhof (PBE)[56] theory level with D3 dispersion[57] (Becke-Johnson damping[58]) and dipole corrections. The projector-augmented wave (PAW)[59,60] method was used to model core electrons. Conventional valence configurations were employed for all elements. An energy cutoff of 400 eV (600 eV for bulk) and gaussian smearing of 0.1 eV width were used for all structures. The SCF iterations were converged to 10^{-6} eV and geometries were optimized to 0.03eV/Å (0.01 eV/Å) for slab (bulk) calculations. All DFT calculations were performed with the Vienna ab-initio simulation package (VASP, version 5.4.1).[61,62] Bader charge analysis[63] was performed using the Henkelman *et al.* implementation.[64] The Visualisation for Electronic and Structural Analysis (VESTA) package[65] was employed to visualize structures.

Bulk ceria ($Fm\overline{3}m$) with a calculated lattice constant of 5.462 Å (close to experimental value of 5.411 Å[66]) was used to cleave the (111), (110), and (100) facets for this study. For the (100) facet, the oxygen terminated surface with half the surface oxygens removed to the bottom of the slab was used as reported in literature.[67,68] A vacuum layer 20 Å thick in the direction normal to the surface was used in all cases. Periodicity of (2×2) are employed for all three facets. Each slab is three layers thick (16•CeO$_2$ and 8•CeO$_2$ considered a layer for (110)/(111)and (100), respectively) in which the bottom third of the atomic layers were held fixed to mimic the bulk properties. Monkhorst-Pack k-point sampling of [$3 \times 3 \times 1$] was used for each facet. A +U value of 5 eV on 4f-orbitals of Ce was applied.[69] Effect of +U value on the work function (Table S14) was tested and found to have a neglectable effect on the work functions of CeO$_2$(111) and (110) (varies by < 2%). The oxygen vacancy formation energy was computed from the equation

$$E_{V_O} = E_{CeO_{2-x}} + \frac{x}{2}E_{O_2} - E_{CeO_2} .$$

Author contributions

S. S. carried out the catalyst preparation, characterizations, analysis, tests and drafted the manuscript. S. L. and S. C. carried out the DFT calculations and drafted the manuscript. C. D. and J. U. carried out the XPS, part of TEM and EDS mapping. W. Z. carried out part of the TEM and assisted with the XPS deconvolution. D.G.V., S. L., C. D. and S. S. discussed the results and assisted with the manuscript preparation. D.G.V led the project and revised the paper. All authors reviewed and commented on the manuscript.

Data availability

All data generated in this study are provided as supplementary dataset.

Supplementary Information accompanies this paper at http://www.nature.com/naturecommunications

Competing interests: The authors declare no competing interests.

References

1. Wan, W. *et al.* Controlling reaction pathways of selective C–O bond cleavage of glycerol. *Nature Communications* **9**, 4612 (2018).
2. Pan, X., Jiao, F., Miao, D. & Bao, X. Oxide–Zeolite-Based Composite Catalyst Concept That Enables Syngas Chemistry beyond Fischer–Tropsch Synthesis. *Chemical Reviews* **121**, 6588–6609 (2021).
3. Pfriem, N. *et al.* Role of the ionic environment in enhancing the activity of reacting molecules in zeolite pores. *Science* **372**, 952–957 (2021).
4. Goulas, K. A., Mironenko, A. V. & Jenness, G. R. Fundamentals of C–O bond activation on metal oxide catalysts. *Nat Catal* **2**, 269–276 (2019).
5. Fu, J. *et al.* C–O bond activation using ultralow loading of noble metal catalysts on moderately reducible oxides. *Nature Catalysis* **3**, 446–453 (2020).
6. Sutton, A. D. *et al.* The hydrodeoxygenation of bioderived furans into alkanes. *Nature Chemistry* **5**, 428–432 (2013).
7. Luo, Z. *et al.* Transition metal-like carbocatalyst. *Nature Communications* **11**, 4091 (2020).
8. Li, J. *et al.* Chemoselective Hydrodeoxygenation of Carboxylic Acids to Hydrocarbons over Nitrogen-Doped Carbon–Alumina Hybrid Supported Iron Catalysts. *ACS Catalysis* **9**, 1564–1577 (2019).
9. Foster, A. J., Do, P. T. M. & Lobo, R. F. The Synergy of the Support Acid Function and the Metal Function in the Catalytic Hydrodeoxygenation of m-Cresol. *Topics in Catalysis* **55**, 118–128 (2012).
10. Jin, Z. *et al.* Metal-acid interfaces enveloped in zeolite crystals for cascade biomass hydrodeoxygenation. *Applied Catalysis B: Environmental* **254**, 560–568 (2019).
11. Zhao, Z. *et al.* Solvent-mediated charge separation drives alternative hydrogenation path of furanics in liquid water. *Nature Catalysis* **2**, 431–436 (2019).
12. Mironenko, A. V. & Vlachos, D. G. Conjugation-Driven "Reverse Mars–van Krevelen"-Type Radical Mechanism for Low-Temperature C–O Bond Activation. *J. Am. Chem. Soc.* **138**, 8104–8113 (2016).
13. Tauster, S. J., Fung, S. C. & Garten, R. L. Strong metal-support interactions. Group 8 noble metals supported on titanium dioxide. *Journal of the American Chemical Society* **100**, 170–175 (1978).
14. Singh, A. K., Pande, N. K. & Bell, A. T. Electron microscopy study of the interactions of rhodium with titania. *Journal of Catalysis* **94**, 422–435 (1985).
15. Logan, A. D., Braunschweig, E. J., Datye, A. K. & Smith, D. J. Direct observation of the surfaces of small metal crystallites: rhodium supported on titania. *Langmuir* **4**, 827–830 (1988).

387 16. Dong, J. *et al.* Reaction-Induced Strong Metal–Support Interactions between Metals and Inert Boron Nitride Nanosheets. *Journal of*
388 *the American Chemical Society* **142**, 17167–17174 (2020).
389 17. Tang, H. *et al.* Classical strong metal–support interactions between gold nanoparticles and titanium dioxide. *Science Advances* **3**,
390 e1700231 (2017).
391 18. Wang, H. *et al.* Strong metal–support interactions on gold nanoparticle catalysts achieved through Le Chatelier's principle. *Nature*
392 *Catalysis* **4**, 418–424 (2021).
393 19. Matsubu, J. C. *et al.* Adsorbate-mediated strong metal–support interactions in oxide-supported Rh catalysts. *Nature Chemistry* **9**,
394 120–127 (2017).
395 20. Tang, M. *et al.* Facet-Dependent Oxidative Strong Metal-Support Interactions of Palladium–TiO2 Determined by In Situ
396 Transmission Electron Microscopy. *Angewandte Chemie International Edition* **60**, 22339–22344 (2021).
397 21. Zhang, Y. *et al.* Structure Sensitivity of Au-TiO2 Strong Metal–Support Interactions. *Angewandte Chemie International Edition* **60**,
398 12074–12081 (2021).
399 22. Mai, H.-X. *et al.* Shape-Selective Synthesis and Oxygen Storage Behavior of Ceria Nanopolyhedra, Nanorods, and Nanocubes. *The*
400 *Journal of Physical Chemistry B* **109**, 24380–24385 (2005).
401 23. Jiang, F. *et al.* Insights into the Influence of CeO2 Crystal Facet on CO2 Hydrogenation to Methanol over Pd/CeO2 Catalysts. *ACS*
402 *Catalysis* **10**, 11493–11509 (2020).
403 24. Tan, Z. *et al.* Differentiating Surface Ce Species among CeO2 Facets by Solid-State NMR for Catalytic Correlation. *ACS Catalysis*
404 **10**, 4003–4011 (2020).
405 25. Zhang, Z. *et al.* Metal-Free Ceria Catalysis for Selective Hydrogenation of Crotonaldehyde. *ACS Catalysis* **10**, 14560–14566 (2020).
406 26. Date, N. S., Hengne, A. M., Huang, K. W., Chikate, R. C. & Rode, C. V. Single pot selective hydrogenation of furfural to 2-
407 methylfuran over carbon supported iridium catalysts. *Green Chemistry* **20**, 2027–2037 (2018).
408 27. Komai, S., Yazawa, Y., Satsuma, A. & Hattori, T. Determination of Metal Dispersion of Pt/CeO2 Catalyst by CO-pulse Method.
409 *Journal of the Japan Petroleum Institute* **48**, 173–177 (2005).
410 28. Bernal, S. *et al.* HREM study of the behaviour of a Rh/CeO2 catalyst under high temperature reducing and oxidizing conditions.
411 *Catalysis Today* **23**, 219–250 (1995).
412 29. Li, S. *et al.* Tuning the Selectivity of Catalytic Carbon Dioxide Hydrogenation over Iridium/Cerium Oxide Catalysts with a Strong
413 Metal-Support Interaction. *Angew Chem Int Ed Engl* **56**, 10761–10765 (2017).
414 30. Lin, J. *et al.* More active Ir subnanometer clusters than single-atoms for catalytic oxidation of CO at low temperature. *AIChE Journal*
415 **63**, 4003–4012 (2017).
416 31. Ding, K. *et al.* Identification of active sites in CO oxidation and water-gas shift over supported Pt catalysts. *Science* **350**, 189–192
417 (2015).
418 32. Zhang, Z. & Yates, J. T. Band Bending in Semiconductors: Chemical and Physical Consequences at Surfaces and Interfaces. *Chem.*
419 *Rev.* **112**, 5520–5551 (2012).
420 33. Fu, Q. & Wagner, T. Interaction of nanostructured metal overlayers with oxide surfaces. *Surface Science Reports* **62**, 431–498
421 (2007).
422 34. Pérez-Bailac, P., Lustemberg, P. G. & Ganduglia-Pirovano, M. V. Facet-dependent stability of near-surface oxygen vacancies and
423 excess charge localization at CeO2 surfaces. *Journal of Physics: Condensed Matter* **33**, 504003 (2021).
424 35. Greiner, M. T., Chai, L., Helander, M. G., Tang, W.-M. & Lu, Z.-H. Transition Metal Oxide Work Functions: The Influence of
425 Cation Oxidation State and Oxygen Vacancies. *Advanced Functional Materials* **22**, 4557–4568 (2012).
426 36. Zhang, R., Chutia, A., Sokol, A. A., Chadwick, D. & Catlow, C. R. A. A computational investigation of the adsorption of small
427 copper clusters on the CeO2(110) surface. *Phys. Chem. Chem. Phys.* **23**, 19329–19342 (2021).
428 37. Luo, J. *et al.* Mechanisms for High Selectivity in the Hydrodeoxygenation of 5-Hydroxymethylfurfural over PtCo Nanocrystals. *ACS*
429 *Catalysis* **6**, 4095–4104 (2016).
430 38. Wang, C. *et al.* Mechanistic Study of the Direct Hydrodeoxygenation of m-Cresol over WOx-Decorated Pt/C Catalysts. *ACS*
431 *Catalysis* **8**, 7749–7759 (2018).
432 39. Abid, M., Paul-Boncour, V. & Touroude, R. Pt/CeO2 catalysts in crotonaldehyde hydrogenation: Selectivity, metal particle size and
433 SMSI states. *Applied Catalysis A: General* **297**, 48–59 (2006).
434 40. Chen, L. *et al.* Insights into the Mechanism of Methanol Steam Reforming Tandem Reaction over CeO2 Supported Single-Site
435 Catalysts. *J Am Chem Soc* **143**, 12074–12081 (2021).
436 41. Yang, J. *et al.* Oxygen Vacancy Promoted O2 Activation over Perovskite Oxide for Low-Temperature CO Oxidation. *ACS Catalysis*
437 **9**, 9751–9763 (2019).
438 42. Tang, Q., Jiang, L., Liu, J., Wang, S. & Sun, G. Effect of Surface Manganese Valence of Manganese Oxides on the Activity of the
439 Oxygen Reduction Reaction in Alkaline Media. *ACS Catalysis* **4**, 457–463 (2014).
440 43. Watanabe, S., Ma, X. & Song, C. Characterization of Structural and Surface Properties of Nanocrystalline TiO2−CeO2 Mixed Oxides
441 by XRD, XPS, TPR, and TPD. *The Journal of Physical Chemistry C* **113**, 14249–14257 (2009).
442 44. Jones, J. *et al.* Thermally stable single-atom platinum-on-ceria catalysts via atom trapping. *Science* **353**, 150–154 (2016).
443 45. Zhang, N. *et al.* Lattice oxygen activation enabled by high-valence metal sites for enhanced water oxidation. *Nature Communications*
444 **11**, 4066 (2020).
445 46. Pereira-Hernández, X. I. *et al.* Tuning Pt-CeO2 interactions by high-temperature vapor-phase synthesis for improved reducibility of
446 lattice oxygen. *Nature Communications* **10**, 1358 (2019).
447 47. Jenness, G. R. & Vlachos, D. G. DFT Study of the Conversion of Furfuryl Alcohol to 2-Methylfuran on RuO2 (110). *J. Phys. Chem.*
448 *C* **119**, 5938–5945 (2015).
449 48. Du, X. *et al.* Size-dependent strong metal-support interaction in TiO2 supported Au nanocatalysts. *Nature Communications* **11**, 5811
450 (2020).
451 49. Han, B. *et al.* Strong Metal–Support Interactions between Pt Single Atoms and TiO2. *Angewandte Chemie International Edition* **59**,
452 11824–11829 (2020).
453 50. Dong, J., Fu, Q., Jiang, Z., Mei, B. & Bao, X. Carbide-Supported Au Catalysts for Water–Gas Shift Reactions: A New Territory for
454 the Strong Metal–Support Interaction Effect. *Journal of the American Chemical Society* **140**, 13808–13816 (2018).

455   51.   Polo-Garzon, F. *et al.* In Situ Strong Metal–Support Interaction (SMSI) Affects Catalytic Alcohol Conversion. *ACS Catalysis* **11**,
456   1938–1945 (2021).
457   52.   Weerachawanasak, P. *et al.* Effect of strong metal–support interaction on the catalytic performance of Pd/TiO2 in the liquid-phase
458   semihydrogenation of phenylacetylene. *Journal of Catalysis* **262**, 199–205 (2009).
459   53.   Zhang, Y. *et al.* Tuning selectivity of CO2 hydrogenation by modulating the strong metal–support interaction over Ir/TiO2 catalysts.
460   *Green Chemistry* **22**, 6855–6861 (2020).
461   54.   Huang, R., Kwon, O., Lin, C. & Gorte, R. J. The effects of SMSI on m-Cresol hydrodeoxygenation over Pt/Nb2O5 and Pt/TiO2.
462   *Journal of Catalysis* **398**, 102–108 (2021).
463   55.   Cargnello, M. *et al.* Control of Metal Nanocrystal Size Reveals Metal-Support Interface Role for Ceria Catalysts. *Science* **341**, 771
464   (2013).
465   56.   Perdew, J. P., Burke, K. & Ernzerhof, M. Generalized Gradient Approximation Made Simple. *Phys. Rev. Lett.* **78**, 1396–1396 (1997).
466   57.   Grimme, S., Antony, J., Ehrlich, S. & Krieg, H. A consistent and accurate ab initio parametrization of density functional dispersion
467   correction (DFT-D) for the 94 elements H-Pu. *The Journal of chemical physics* **132**, 154104 (2010).
468   58.   Grimme, S., Ehrlich, S. & Goerigk, L. Effect of the damping function in dispersion corrected density functional theory. *Journal of*
469   *Computational Chemistry* **32**, 1456–1465 (2011).
470   59.   Kresse, G. & Joubert, D. From ultrasoft pseudopotentials to the projector augmented-wave method. *Phys. Rev. B* **59**, 1758–1775
471   (1999).
472   60.   Blöchl, P. E. Projector augmented-wave method. *Phys. Rev. B* **50**, 17953–17979 (1994).
473   61.   Kresse, G. & Furthmüller, J. Efficiency of ab-initio total energy calculations for metals and semiconductors using a plane-wave basis
474   set. *Computational Materials Science* **6**, 15–50 (1996).
475   62.   Kresse, G. & Furthmüller, J. Efficient iterative schemes for ab initio total-energy calculations using a plane-wave basis set. *Phys. Rev.*
476   *B* **54**, 11169–11186 (1996).
477   63.   Bader, R. F. A quantum theory of molecular structure and its applications. *Chemical Reviews* **91**, 893–928 (1991).
478   64.   Henkelman, G., Arnaldsson, A. & Jónsson, H. A fast and robust algorithm for Bader decomposition of charge density. *Computational*
479   *Materials Science* **36**, 354–360 (2006).
480   65.   Momma, K. & Izumi, F. VESTA: a three-dimensional visualization system for electronic and structural analysis. *Journal of Applied*
481   *Crystallography* vol. 41 653–658 (2008).
482   66.   Kümmerle, E. A. & Heger, G. The Structures of C–Ce2O3+δ, Ce7O12, and Ce11O20. *Journal of Solid State Chemistry* **147**, 485–500
483   (1999).
484   67.   Pan, Y. *et al.* Ceria Nanocrystals Exposing Wide (100) Facets: Structure and Polarity Compensation. *Advanced Materials Interfaces*
485   **1**, 1400404 (2014).
486   68.   Capdevila-Cortada, M. & López, N. Entropic contributions enhance polarity compensation for CeO2(100) surfaces. *Nature Materials*
487   **16**, 328–334 (2017).
488   69.   Nolan, M. Hybrid density functional theory description of oxygen vacancies in the CeO2 (110) and (100) surfaces. *Chemical Physics*
489   *Letters* **499**, 126–130 (2010).
490
491
492
493